COMMUNICATIONS

One Micrometer Resolution NMR Microscopy

Seung-Cheol Lee,* Kiseong Kim,* Junghyun Kim,* Soonchil Lee,* Jeong Han Yi,† Sung Woo Kim,‡
Kwon-Soo Ha,‡ and Chaejoon Cheong§

*Department of Physics, Korea Advanced Institute of Science and Technology, Taejon 305-701, Korea; †Department of Biomedical Engineering,
Konkuk University, Choongju 380-701, Korea; and ‡Biomolecule Research Team and §Magnetic Resonance Team,
Korea Basic Science Institute, Taejon 305-333, Korea

We obtained a magnetic resonance image of 1 μm resolution and 75 μm^3 voxel volume for a phantom filled with hydrocarbon oil within an hour at 14.1 T. For this work, a specially designed probe with a high sensitivity RF coil and gradient coils generating over 1000 G/cm was built. The optimal pulse sequence was analyzed in consideration of the bandwidth, diffusion coefficients, and T_1 and T_2 relaxations of the medium. The system was applied to the *in vivo* imaging of a geranium leaf stem to get the images of 2 μm resolution and 200 μm^3 voxel volume.   © 2001 Academic Press

Key Words: NMR microscopy; micron resolution; diffusion analysis; high magnetic field; high gradient field.

INTRODUCTION

The resolution in NMR imaging is one of the key parameters in revealing microstructures of objects, and enhancing the resolution has been the main interest of many NMR researchers (*1*). Since Hedges' early work on developing the NMR microscope (*2*), Aguayo *et al.* (*3*) first observed single cell images and many other NMR microscopy experiments followed (*4–8*). Cho *et al.* have reached the in-plane resolution of 4^2 μm^2 (*4*), and Zhou *et al.* have reached the isotropic voxel volume resolution of $6.4^3 \mu$m$^3 \approx 260$ μm^3 (*6*). While there has been much endeavor since then, the highest resolutions in pixels and voxels have remained at these values until recently. This paper addresses the work on NMR imaging with 1 μm resolution, which has a symbolic significance as a biological cell size.

The most significant factor limiting the resolution is poor signal-to-noise ratio (SNR) of an NMR signal decreasing with voxel volume, because NMR signal amplitude is proportional to the number of nuclear spins in a voxel. Other limiting factors include the effects of diffusion, transverse relaxation, and susceptibility (*1*). The most conventional method to increase SNR and voxel resolution is using a high magnetic field and microcoils, because in ideal cases, SNR is proportional to the 7/4th power of the static magnetic field and inversely proportional to the diameter of an RF coil in the high frequency region (*9, 10*). Sev-

eral sophisticated methods have been also tried to enhance SNR. Superconducting RF coils were used to reduce coil noise (*11, 12*), and the cross-relaxation between the aqueous solution and hyperpolarized xenon (*13*), or the dynamic nuclear polarization with radicals (*14*), was used to enhance nuclear magnetization. Each of these methods is promising in some sense, but impractical for general-purpose microscopy for now. Superconducting wire can be used only for surface and helmholtz coils and has given voxel resolution of $\sim 20^3$ μm^3 at best. The method using optically pumped xenon gas has increased SNR by about 10%. Dynamic nuclear polarization with radicals was recently examined to determine whether it has the potential to produce nuclear polarization larger than the thermally equilibrated polarization obtained from the highest magnetic field of today.

We obtained NMR images with 1 μm resolution and 75 μm^3 voxel volume using the conventional method and a specially built microscopy probe at 14.1 T. The probe is composed of a high sensitivity RF tank circuit with a microcoil and gradient coils yielding gradient strength over 1000 G/cm. The pulse sequence and imaging parameters were optimized to achieve as high SNR as possible by reducing the signal attenuation effects of diffusion and relaxation.

EXPERIMENTAL

The experiment was carried out using a Bruker DMX 600 spectrometer equipped with a 14.1-T vertical standard bore magnet and a gradient amplifier capable of making 40 A current flow at maximum in the x, y, and z coils. The microscopy probe was designed to suit submicrometer resolution imaging. To get a high Q-factor and high gradient field strength, the RF tank circuit was constructed as compactly as possible. A solenoidal type microcoil of about 500-μm diameter was loaded on top of the miniature size variable capacitors (NMA1T4HV, Voltronics Corp.) (Fig. 1). The overall diameter of the tank circuit constructed in the Teflon holder which was located inside the Golay type gradient coil, was 12.8 mm. The RF insert was isolated from the gradient coil by O-rings. The Q-factor of the tank circuit
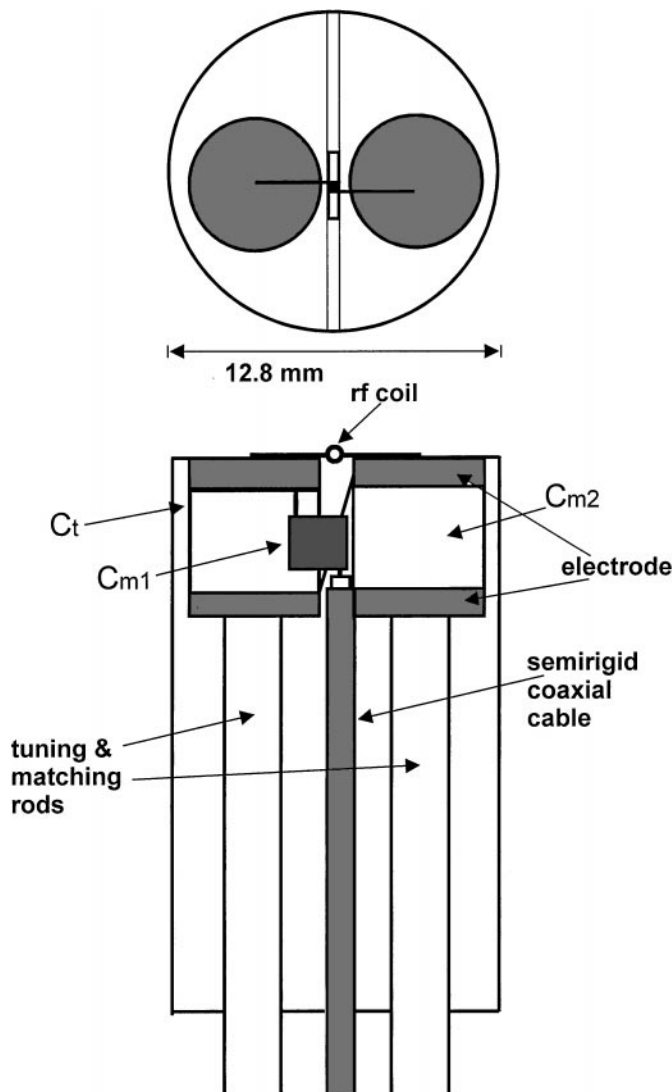
FIG. 1. The RF tank circuit of our homebuilt NMR microscopy probe. A micro RF coil is located on top of the variable capacitors. C_t is the variable capacitor for parallel tuning, and C_{m1} and C_{m2} are fixed and variable matching capacitors, respectively.

measured by a network analyzer was 60, which decreases by about 10% when loaded.

The type of z-gradient was a Maxwell pair. The advantages a Golay type coil has over a quadrupolar type coil in NMR microscopy are that it can provide relatively large space for the RF tank circuit, and the geometry of the cooling system is simple because the coil axis is parallel to the static field. Since the whole tank circuit can be located inside the bore of the gradient coil, the connection length between the RF coil and the capacitors can be made as short as possible to get high Q- and filling factors. When a microcoil is used, usually the connection length decides the filling factor. Gradient coil cooling would be inevitable for imaging experiments with submicrometer resolution.

Enamel-coated 0.40-mm-diameter copper wire was wound 36, 40, and 75 turns for the x, y, and z gradient coils on a Derlin

former to produce 1360, 1120, and 1230 G/cm at 40 A, respectively. The outer diameter of the gradient coil unit was 39.7 mm, which is the accessible bore diameter of the magnet. Although the gradient coil is rather close to the inner bore of the magnet, no artifacts due to eddy current were observed under our experimental conditions. This is because the ratio of the sample size to the radius of the gradient is small, less than 1%. A Pt100 temperature sensor (Lakeshore Cryotronics, Inc.) is attached to the gradient windings for monitoring 15°C water flow at 0.5 atm around the gradient coil. When a large gradient pulse is used in a high static field, the mechanical rigidity of the gradient coil is important. Normal epoxy, which is generally used to form a gradient coil, is not suitable for a 1 μm resolution experiment because it cannot effectively transfer the heat generated by the gradient coil to cooling water during a long experiment with a short repetition time. When the gradient coils are not cooled effectively, the generated heat makes the epoxy soft and the mechanical hardness of the gradient coil is not sustained any longer. To overcome this problem, we increased the thermal conductivity of epoxy by mixing it with aluminum powder. This provided enough mechanical rigidity for the experiment, and the effect of vibration was never observed in our experiments, regardless of gradient strength. The temperature rise of the gradient coil unit during the experiments in this paper was less than 2°.

The phantom prepared for the 1 μm resolution experiment is a cylinder filled with hydrocarbon composite oil (Kyoungin Energy Co., Korea). Polyurethane-coated 95-μm-diameter copper wire was wound 5 turns tightly around a glass tube of outer diameter 450 μm and inner diameter 275 μm. Two capillaries of 110 μm outer diameter were inserted in the tube. To find the optimal experiment condition, the spin–lattice and spin–spin relaxation times and the diffusion coefficient of the oil were measured by the inversion recovery, spin echo, and pulsed gradient spin echo methods, respectively. The measured values were 630 ms, 24 ms, and 1.7×10^{-7} cm^2 s^{-1} at 17.5°C, respectively. For comparison, the diffusion coefficient of pure water was also measured at the same temperature with the result of 1.8×10^{-5} cm^2 s^{-1}, which coincides with the value in the literature (15). It is worthwhile to note that the diffusion coefficient of the hydrocarbon oil is two orders of magnitude smaller than that of water. This small diffusion coefficient reduces the signal attenuation due to diffusion.

The object used for biological tissue imaging was a geranium leaf stem. Since the natural cells have long spin–lattice relaxation times ($T_1 \approx 1.5$ s), the leaf stem was cut and immersed in a 50 mM CuSO$_4$ solution for 1 h to shorten the relaxation time. The resultant T_1 value was 83 ms and T_2 was 8.8 ms. The average diffusion coefficient of the leaf stem was 4.6×10^{-6} cm^2 s^{-1}. The stem was inserted in a glass tube of outer diameter of about 600 μm and inner diameter about 350 μm under an optical microscope. A polyurethane-coated 140-μm-diameter copper wire was wound 5 turns around the tube.

The field of view (FOV) and slice thickness for the image of the artificial phantom were 500 and 75 μm, respectively, and those for the geranium were 1 mm and 50 μm, respectively.

The matrix size was 512 × 512, and the repetition time was set to $1.25 \times T_1$, which gave the maximum SNR in a given time, consistent with the theoretical calculation. The optimal pulse sequence and imaging parameters were found by the analysis described in the next section.

OPTIMIZATION OF THE PULSE SEQUENCE

The pulse sequence used in the experiment is depicted in Fig. 2. This is basically a spin echo sequence modified to make the echo time as short as possible. It reduces the signal attenuation due to T_2 relaxation and diffusion, which become more and more important as pixel size becomes smaller. For the purpose, a hard 180° RF pulse, the largest possible gradients, and asymmetric data acquisition were employed. The ratio δ_2/T_{acq} was set to (64/512) for the imaging of the artificial phantom with 1 μm resolution and to (96/512) for the imaging of the plant with 2 μm resolution. The image was reconstructed from the asymmetrically acquired data using the iterative partial Fourier reconstruction technique with five iterations (16). The reading gradient amplitudes were adjusted so that the gradient echo coincides with the RF echo to prevent image degradation from field inhomogeneity, that is, $g_1\delta_1 = g_2\delta_2$. Among the various gradients, the phase encoding gradient was the largest, set to 1000 G/cm. Both the read-dephase gradient and the phase encoding gradient began just after the slice selection gradient g_{S1} and ended 100 μs before the 180° RF pulse. The read ac-

quisition gradient started just after the crusher gradient g_{S2} with duration 200 μs in the slice direction, which was located just after the 180° pulse. The minimum duration required for the gradient switching is 100 μs. The sinc 90° pulse was 1 ms, and the hard 180° pulse was 16 μs.

The signal attenuation due to diffusion is generally given as (17)

$$A(t) = \exp\left[-\gamma^2 D \int_0^t dt' \left(\int_0^{t'} dt'' \mathbf{G}(t'')\right)^2\right], \qquad [1]$$

where γ is the gyromagnetic ratio, D is the diffusion coefficient of a sample, and $\mathbf{G}(t)$ is the time-dependent magnetic field gradient. For the pulse sequence in Fig. 2, the signal attenuation at echo by the reading gradient is calculated as

$$A_R(\text{Diff}) = \exp\left[-D\gamma^2 g_2^2 \delta_2^2\left(\Delta - \frac{2}{3}\delta_1 + \frac{1}{3}\delta_2\right)\right]. \qquad [2]$$

When $g_1 = g_2$ and $\delta_1 = \delta_2$, the equation reduces to the well-known Stejskal–Tanner equation (18). The attenuation by the selection gradient, $A_S(\text{Diff})$, is similarly calculated by substituting $g_2 = g_{S2}$, $\delta_1 = \delta_{S1}$, $\delta_2 = \delta_{S2}$, and $\Delta = \Delta_s$ in Eq. [2]. The attenuation by the phase encoding gradient is neglected because the phase gradient is near zero when signal amplitude is significant. The total diffusive attenuation is the product of the attenuation by the read and selection gradients. At echo there is also the signal reduction by T_2 relaxation,

$$A(T_2) = \exp(-T_E/T_2). \qquad [3]$$

Since the RMS noise amplitude is inversely proportional to the square root of bandwidth (BW), the SNR can be written as

$$\text{SNR} \propto A(\text{total}) = \frac{1}{\sqrt{BW}} A_R(\text{Diff}) A_S(\text{Diff}) A(T_2). \qquad [4]$$

All of the attenuation terms increase with decreasing echo time or increasing bandwidth for a fixed resolution because bandwidth decides gradient amplitudes. Therefore, the SNR in Eq. [4] shows a maximum as a function of bandwidth. Sometimes, however, this maximum condition cannot be satisfied due to hardware restrictions depending on imaging conditions. The finite width of the 90° RF pulse and dephase gradients decides the minimum echo time and the corresponding bandwidth BW_0. SNR should be estimated separately for $BW \leq BW_0$ and $BW > BW_0$. When the bandwidth is larger than BW_0, Eq. [4] is analyzed with the echo time fixed as its minimum value.

The detailed analysis of Eq. [4] as a function of bandwidth and various imaging parameters is given in the Appendix. Figure 3 shows the results for the oil and plant with the imaging conditions described above and that for water for comparison. The
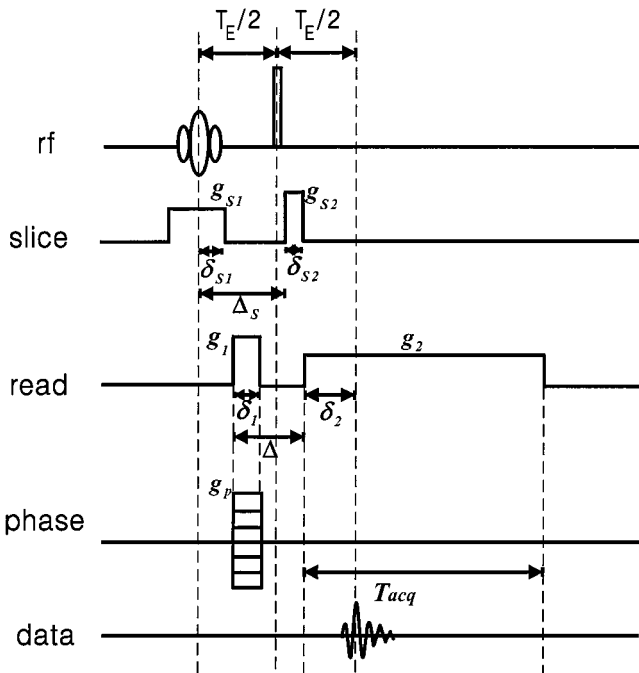
FIG. 2. Pulse sequence used for the micrometer resolution NMR imaging. Various parameters were optimized to get the best SNR for given diffusion coefficients and relaxation times.
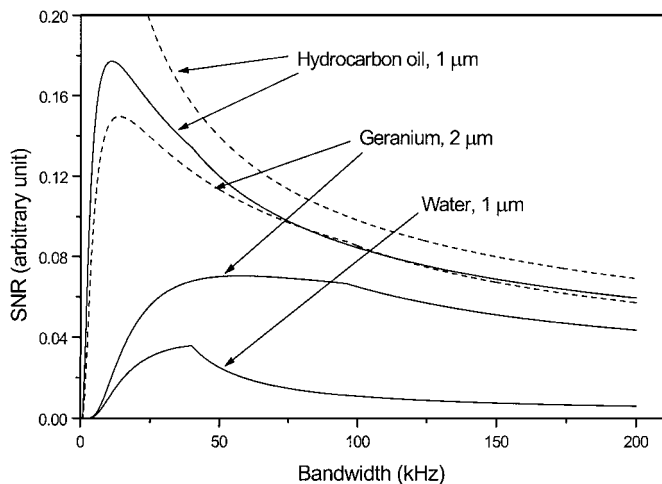
FIG. 3. Total signal attenuation A(total) (solid line) and attenuation due to diffusion (dashed line) for various media and resolutions.

solid lines represent A(total), and the dashed lines represent the diffusive attenuation, that is, Eq. [4] without the T_2 relaxation term. In the figure, it is clear that the T_2 relaxation effect cannot be ignored for liquid samples in micrometer resolution in general. Each line has a discontinuity in its slope at BW_0 because the echo time is fixed as its minimum value for $BW > BW_0$ as described above. While the maximum SNR appears below BW_0 for the hydrocarbon oil with 1 μm resolution and the geranium with 2 μm resolution, the maximum is at BW_0 for pure water with 1 μm resolution. For hydrocarbon oil in the 1^2 μm^2 pixel condition, A(total)$_{max}$, is 0.18 at 11 kHz. However, due to the software limitations, the bandwidth actually adopted for the imaging experiment was 25 kHz, where A(total) is 0.16. The advantage of choosing hydrocarbon oil as an imaging medium in micrometer resolution imaging is obvious from the fact that A(total)$_{max}$ of hydrocarbon oil is 5 times larger than that of water under the same condition. A normal spin echo sequence with soft 180° pulse and symmetric data acquisition would give an A(total)$_{max}$ of 0.043 for hydrocarbon oil and 10^{-24} for water. This indicates that adequate selection of the pulse sequence and medium is critical in achieving 1^2 μm^2 pixel imaging. The attenuation due to the selection gradient is negligible for hydrocarbon oil, but decreases SNR by about 10% for water. The A(total)$_{max}$ of geranium in the 2^2 μm^2 pixel condition is 0.070 at 58 kHz.

REPRESENTATIVE IMAGES AND DISCUSSION

Figure 4a shows the phantom image of a tube with two capillaries in it. The slice thickness is 75 μm and the in-plane pixel size is 1^2 μm^2. The echo time and repetition time were 5.5 and 800 ms, respectively, and the number of average was 8, resulting in the total imaging time of 56 min. The image shown in the figure is a part of the original image of 500 μm FOV and a

512 × 512 matrix. The vertical direction of the image is the read direction, and the horizontal direction is the phase direction. The diameter of the large circle in the image is 275 μm, which is the inside of the tube. The diameter and thickness of two capillaries are about 110 and 16 μm, respectively. The SNR of the image was 4.6, which was calculated by dividing the average signal amplitude by the standard deviation in the region indicated by a box. The blurring in the readout direction is mainly the effect of susceptibility. It is observed that the blurring is diminished if the gradient is increased to overcome the inhomogeneity due to susceptibility. The blurring due to asymmetric sampling is eliminated by the iterative partial Fourier technique except in the region where phase changes abruptly. The phase map of the image in Fig. 4 showed no region of abrupt phase change. Figure 4b is a cut view of the image along the horizontal line in the image. The top figure shows a cut view of the full 512 pixels, and the bottom shows a part enlarged. The bottom figure clearly shows that the signal amplitude jumps abruptly at the 124th and 143th pixels, indicating that the real resolution of the image is
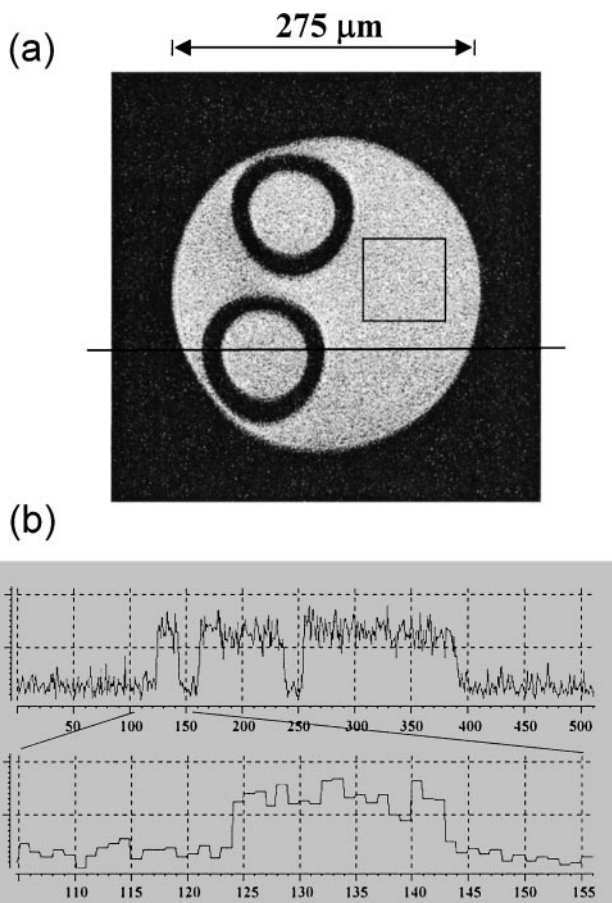

FIG. 4. (a) The image of a tube with two capillaries in it with voxel size of $1 \times 1 \times 75$ μm^3: $T_E = 5.5$ ms, $T_R = 800$ ms, number of averages = 8, total imaging time = 56 min. (b) A cut view of the image along the horizontal line: a full cut view with 512 points (top) and an enlarged view of the region where signal intensity varies suddenly (bottom).
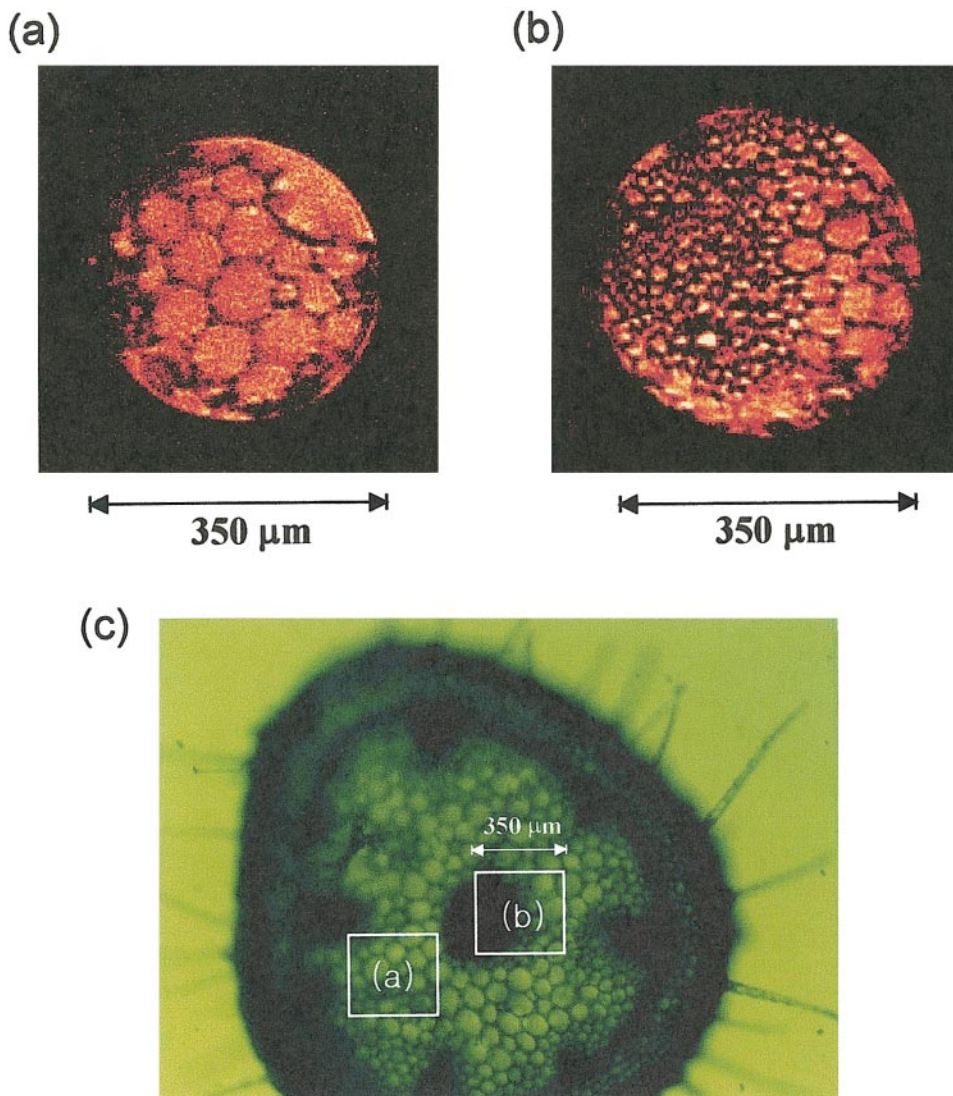
FIG. 5. The images of geranium leaf stems in the large (a) and small (b) cell regions with voxel size of $2 \times 2 \times 50 \ \mu m^3$: $T_E = 4.2$ ms, $T_R = 200$ ms, number of averages = 32, total imaging time = 56 min. (c) An optical microscope image of the geranium leaf stem.

close to the pixel size. Diffusion effect on an image is mostly detected by the image distortion near edges. In our image, this kind of distortion is not observed in consistence with theory, which predicts that $A_R(\text{Diff})$ deviates from 1 only by 0.017 for the hydrocarbon oil with the imaging parameters used in the experiment.

Figures 5a and 5b show the images of the leaf stem cells obtained using our microscopy system. The slice thickness is 50 μm and the in-plane pixel size is $2^2 \ \mu m^2$. The figures are also parts of the original image of 1 mm FOV and a 512×512 matrix. The echo time and repetition time were 4.2 and 200 ms, respectively, and the number of averages was 32, resulting in the total experiment time of 56 min. The cells of the leaf stem are cylindrical in shape and 100–300 μm long depending on the cell size. The optical image in Fig. 5c shows a representative

geranium leaf stem. The cell size in Fig. 5a is 30–80 μm, and the spacing between cells is about 6 μm. The MRI image in Fig. 5b clearly shows smaller cells ($\sim$14 μm) which are not observed well by optical means. The SNR of the images in Figs. 5a and 5b was 8.5.

In conclusion, we obtained 1 μm resolution images whose voxel size is 75 μm^3 at 14.1 T with our specially designed microscopy probe. The RF tank circuit was made as compactly as possible to have high Q- and filling factors and the gradient coils generate over 1000 G/cm. The pulse sequence was optimized for given diffusion coefficients, T_2 relaxation times, and other imaging conditions. This work demonstrates the feasibility of submicrometer resolution NMR microscopy with current technology, and the emerging new technologies are expected to accelerate the resolution enhancement further.

APPENDIX

Let us look into the parameters in Fig. 2. As the spectral bandwidth increases, g_2 increases and δ_2 and T_E decrease in a given resolution. But since the $90°$ pulse length and the phase gradient duration δ_1 do not vary with bandwidth, T_E reaches the minimum at the bandwidth BW_0. When the bandwidth is equal to or larger than BW_0, T_E remains at that minimum value. Considering that the time between g_1 and $180°$ pulse is 0.1 ms, therefore,

$$
\begin{aligned}
T_E &= 2(\delta_{S2} + \delta_2) \quad \text{for BW} \leq BW_0 \\
&= 2(\delta_{S1} + \delta_1 + 0.1 \text{ ms}) \quad \text{for BW} > BW_0, \quad [5] \\
\Delta &= \delta_1 + 0.1 \text{ ms} + \delta_{S2} \quad \text{for BW} \leq BW_0 \\
&= \delta_1 + 0.1 \text{ ms} + T_E/2 - \delta_2 \\
&= 0.2 \text{ ms} + \delta_{S1} + 2\delta_1 - \delta_2 \quad \text{for BW} > BW_0, \quad [6]
\end{aligned}
$$

and BW_0 is calculated as

$$
BW_0 = \frac{MTX \cdot R}{0.4 \text{ ms} + \frac{\pi \cdot MTX}{\gamma g_p FOV}}, \quad [7]
$$

where MTX is the matrix size of the image, $R = \delta_2/T_{acq}$, g_p is the maximum gradient amplitude used for phase encoding, and all other parameters are as defined in Fig. 2.

Inserting the parameters into Eqs. [2] and [3], we obtain the following. When $BW \leq BW_0$,

$$
A_R(\text{Diff}) = \exp\left[-\alpha \left(\frac{MTX}{3BW} R + \beta \right) \right], \quad [8]
$$

$$
A_S(\text{Diff}) = \exp\left[-\xi \left(\frac{MTX}{BW} R + \eta \right) \right], \quad [9]
$$

$$
A(T_2) = \exp\left[-2\left(\frac{MTX}{BW} R + \delta_{S2} \right) \Big/ T_2 \right], \quad [10]
$$

where

$$
\alpha = D \left(\frac{2\pi \cdot MTX}{FOV} R \right)^2,
$$

$$
\beta = \frac{\pi \cdot MTX}{3\gamma g_p \cdot FOV} + \delta_{S2} + 0.1 \text{ ms},
$$

$$
\xi = D\gamma^2 g_{S2}^2 \delta_{S2}^2, \quad \eta = -\frac{2}{3}\delta_{S1} + \frac{4}{3}\delta_{S2},
$$

and therefore,

$$
\begin{aligned}
A(\text{total}) = &\frac{1}{\sqrt{BW}} \exp\left[-\frac{MTX}{BW} R \left(\frac{\alpha}{3} + \xi + \frac{2}{T_2} \right) \right. \\
&\left. - \alpha \cdot \beta - \xi \cdot \eta - \frac{2\delta_{S2}}{T_2} \right]. \quad [11]
\end{aligned}
$$

The maximum point is found by

$$
\begin{aligned}
\frac{dA(\text{total})}{d(BW)} = &BW^{-5/2} \exp\left[-\frac{MTX}{BW} R \left(\frac{\alpha}{3} + \xi + \frac{2}{T_2} \right) - \alpha \cdot \beta \right. \\
&\left. - \xi \cdot \eta - \frac{2\delta_{S2}}{T_2} \right] \left[-\frac{BW}{2} + MTX \cdot R \cdot \left(\frac{\alpha}{3} + \xi \right. \right. \\
&\left. \left. + \frac{2}{T_2} \right) \right] = 0, \quad [12]
\end{aligned}
$$

which gives

$$
BW_m = 2(MTX) \cdot R \cdot \left(\frac{\alpha}{3} + \xi + \frac{2}{T_2} \right). \quad [13]
$$

When $BW > BW_0$,

$$
A_R(\text{Diff}) = \exp\left[-\alpha \left(-\frac{2}{3}\frac{MTX}{BW} R + 4\beta + \delta_{S1} \right. \right. \\
\left. \left. - 4\delta_{S2} - 0.2 \text{ ms} \right) \right], \quad [14]
$$

$$
A_S(\text{Diff}) = \exp(-\xi \cdot \psi), \quad [15]
$$

$$
A(T_2) = \exp\left[-\frac{2(3\beta + \delta_{S1} - 3\delta_{S2} - 0.2 \text{ ms})}{T_2} \right], \quad [16]
$$

$$
A(\text{total}) = \frac{1}{\sqrt{BW}} \exp\left[\frac{2}{3}\alpha \frac{MTX}{BW} R + \kappa \right], \quad [17]
$$

where

$$
\psi = 3\beta - 0.2 \text{ ms} + \frac{1}{3}\delta_{S1} - \frac{8}{3}\delta_{S2},
$$

$$
\begin{aligned}
\kappa = &-\alpha(4\beta + \delta_{S1} - 4\delta_{S2} - 0.2 \text{ ms}) \\
&- \frac{2(3\beta + \delta_{S1} - 3\delta_{S2} - 0.2 \text{ ms})}{T_2} - \xi \cdot \psi. \quad [18]
\end{aligned}
$$

When $BW \leq BW_0$, $A(\text{total})$ increases up to BW_m and decreases afterward. When $BW > BW_0$, $A(\text{total})$ is a monotonously decreasing function. Therefore, the maximum occurs at BW_m if $BW_m \leq BW_0$ and at BW_0 otherwise. The value of $A(\text{total})_{max}$ is

$$
A(\text{total})_{max} = \frac{1}{\sqrt{BW_m}} \exp\left(-\frac{1}{2} - \alpha \cdot \beta - \xi \cdot \eta - \frac{2\delta_{S2}}{T_2} \right) \quad [19]
$$

if $BW_m \leq BW_0$ and

$$
A(\text{total})_{max} = \frac{1}{\sqrt{BW_0}} \exp\left(\frac{2}{3}\alpha \frac{MTX}{BW} R + \kappa \right) \quad [20]
$$

if $BW_m > BW_0$.

ACKNOWLEDGMENTS

REFERENCES

1. P. T. Callaghan, "Principles of Nuclear Magnetic Resonance Microscopy," Clarendon Press, Oxford, 1991.

2. L. K. Hedges, "Microscopic NMR Imaging," Ph.D. dissertation, State University of New York at Stony Brook, 1984.

3. J. B. Aguayo, S. J. Blackband, J. Shoeniger, M. A. Mattingly, and M. Hintermann, Nuclear magnetic resonance of a single cell, *Nature* **322,** 190 (1987).

4. Z. H. Cho, C. B. Ahn, S. C. Juh, H. K. Lee, R. E. Jacobs, S. Lee, J. H. Yi, and J. M. Jo, Nuclear magnetic resonance microscopy with 4 μm resolution: Theoretical study and experimental results, *Med. Phys.* **15,** 815–824 (1988).

5. R. Bowtell, G. D. Brown, P. M. Glover, M. McJury, and P. Mansfield, Resolution of cellular structures by NMR microscopy at 11.7 T, *Philos. Trans. R. Soc. Lond. Biol.* **333,** 457–467 (1990).

6. X. Zhou, C. S. Potter, P. C. Lauterbur, and B. W. Both, NMR imaging with (6.37 μm)^3 isotropic resolution, Abstracts of the Society of Magnetic Resonance in Medicine, 8th Annual Meeting, Amsterdam, The Netherlands p.128 (1989).

7. E. W. McFarland and A. Mortara, Three-dimensional NMR microscopy: Improving SNR with temperature and microcoils, *Magn. Reson. Imag.* **10,** 279–288 (1992).

8. J. S. Schoeniger, N. R. Aiken, E. W. Hsu, and S. J. Blackband, Relaxation and diffusion NMR microscopy of single neurons, *J. Magn. Reson. B* **103,** 261–273 (1994).

9. D. I. Hoult and R. E. Richards, The signal-to-noise ratio of the nuclear magnetic resonance experiment, *J. Magn. Reson.* **24,** 71–85 (1976).

10. T. L. Peck, R. L. Magin, and P. C. Lauterbur, Design and analysis of microcoils for NMR microscopy, *J. Magn. Reson.* **108,** 114–124 (1995).

11. R. D. Black, T. A. Early, P. B. Roemer, O. M. Mueller, A. Mongo-Campero, L. G. Turner, and G. A. Johnson, A high-temperature superconducting receiver for nuclear magnetic resonance microscopy, *Science* **259,** 793–795 (1993).

12. S. E. Hurlston, W. W. Brey, S. A. Suddarth, and G. A. Johnson, A high-temperature superconducting helmholtz probe for microscopy at 9.4 T, *Magn. Reson. Med.* **41,** 1032–1038 (1999).

13. G. Navon, Y. Q. Song, T. Rooms, S. Appeit, E. Taylor, and A. Pines, Enhancement of solution NMR and MRI with laser polarized xenon, *Science* **271,** 1848–1851 (1996).

14. R. A. Wind and J.-H. Ardenkjaer-Larsen, ^{1}H DNP at 1.4 T of water doped with a triarymethyl-based radical, *J. Magn. Reson.* **141,** 347–354 (1999).

15. J. H. Simpson and H. Y. Carr, Diffusion and nuclear spin relaxation in water, *Phys. Rev.* **111,** 1201–1202 (1958).

16. E. M. Haacke, E. D. Lindskog, and W. Lin, A fast iterative partial Fourier technique capable of local phase recovery, *J. Magn. Reson.* **92,** 126–145 (1991).

17. R. F. Karlicek and I. J. Lowe, A modified pulsed field gradient technique for measuring diffusion in the presence of large background gradients, *J. Magn. Reson.* **37,** 75–91 (1980).

18. E. O. Stejskal and J. E. Tanner, Spin diffusion measurements: Spin echoes in the presence of a time-dependent field gradient, *J. Chem. Phys.* **42,** 288–292 (1965).